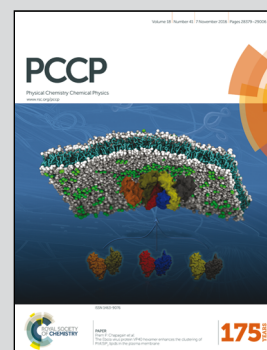


Showcasing work from the laboratory of Prof. Sayantani Ghosh and Prof. Vincent Tung, School of Natural Sciences, University of California, Merced, CA, USA

Title: Low temperature excitonic spectroscopy and dynamics as a probe of quality in hybrid perovskite thin films

The work investigated using low temperature excitonic spectroscopy to shed light on the anomalous photoluminescence emission of organic–inorganic hybrid perovskite thin films at low temperatures, a behavior attributed to the formation of tetragonal nanodomains within the film. We proposed a model based on the observed spectroscopic data, to probe the quality of perovskite films by developing a theoretical route to measure the exciton binding energy in the two temperature regimes, a finding that will be significant for device design and development.

As featured in:



See Sayantani Ghosh *et al.*,  
*Phys. Chem. Chem. Phys.*,  
2016, **18**, 28428.



[www.rsc.org/pccp](http://www.rsc.org/pccp)

Registered charity number: 207890



Cite this: *Phys. Chem. Chem. Phys.*,  
2016, **18**, 28428

# Low temperature excitonic spectroscopy and dynamics as a probe of quality in hybrid perovskite thin films†

Som Sarang,<sup>a</sup> Hidetaka Ishihara,<sup>b</sup> Yen-Chang Chen,<sup>b</sup> Oliver Lin,<sup>b</sup> Ajay Gopinathan,<sup>a</sup> Vincent C. Tung<sup>b</sup> and Sayantani Ghosh\*<sup>a</sup>

We have developed a framework for using temperature dependent static and dynamic photoluminescence (PL) of hybrid organic–inorganic perovskites (PVSKs) to characterize lattice defects in thin films, based on the presence of nanodomains at low temperature. Our high-stability PVSK films are fabricated using a novel continuous liquid interface propagation technique, and in the tetragonal phase ( $T > 120$  K), they exhibit bi-exponential recombination from free charge carriers with an average PL lifetime of  $\sim 200$  ns. Below 120 K, the emergence of the orthorhombic phase is accompanied by a reduction in lifetimes by an order of magnitude, which we establish to be the result of a crossover from free carrier to exciton-dominated radiative recombination. Analysis of the PL as a function of excitation power at different temperatures provides direct evidence that the exciton binding energy is different in the two phases, and using these results, we present a theoretical approach to estimate this variable binding energy. Our findings explain this anomalous low temperature behavior for the first time, attributing it to an inherent fundamental property of the hybrid PVSKs that can be used as an effective probe of thin film quality.

Received 3rd May 2016,  
Accepted 25th July 2016

DOI: 10.1039/c6cp02971j

www.rsc.org/pccp

## 1. Introduction

Organic–inorganic perovskite (PVSK) materials began their foray into the field of photovoltaics (PVs) as sensitizers in solar cells,<sup>1</sup> but have since transitioned to the primary role of an active material in a new generation of hybrid PVs. PVSK solar cells have demonstrated impressive power conversion efficiencies, routinely ranging between 15 and 22%.<sup>2–4</sup> This results from PVSKs possessing a unique combination of properties: the high mobility<sup>5–7</sup> and charge carrier lifetimes<sup>6,8</sup> of inorganic semiconductors,<sup>9</sup> but the flexibility and ease of fabrication of organic materials.<sup>10–13</sup> Researchers in the field are actively engaged in optimizing PV performance enhancement, and in the span of just a couple of years significant progress has been made, including the growth of large high-quality single crystals with micron-scale carrier diffusion lengths,<sup>8,14</sup> improved stability in thin film samples and faster sample preparation techniques.<sup>15</sup> Compared to the effort invested in the PV aspect of PVSKs, there have been fewer investigations in the study of the fundamental properties of hybrid PVSKs. The characteristics that make PVSKs ideal for energy harvesting applications also make them well

suited in the field of opto-electronics,<sup>16</sup> particularly for high efficiency lasers<sup>17</sup> and broadband photo detectors.<sup>18</sup> Recent magneto-optical studies have demonstrated magnetic-field induced state mixing, opening up an entirely new set of possibilities regarding the use of PVSKs in spin-based quantum information platforms.<sup>19</sup> Given the range of possible uses, understanding the fundamentals of charge generation, transport and recombination is essential for not only developing high-efficiency PVs, but also to fully harness the capabilities of hybrid PVSKs for applications in a broader applied context.

Spectroscopic techniques have been key in most of the recent studies that have provided critical insights into the PVSK phase space. This includes a structural phase transition from tetragonal to orthorhombic,<sup>20,21</sup> where the transition temperature depends on the halide composition and concentration.<sup>22,23</sup> For  $\text{CH}_3\text{NH}_3\text{PbI}_{3-x}\text{Cl}_x$  this typically occurs in the range 140–120 K. Optical spectroscopy has shown that the photoluminescence (PL) of the tetragonal phase red-shifts with decreasing temperature, resulting in a positive thermal coefficient, contrary to what is observed in the majority of semiconductors.<sup>20,22</sup> This emission is homogeneously broadened,<sup>18</sup> and has long recombination times on the order of hundreds of nanoseconds.<sup>23,24</sup> The onset of the orthorhombic structure at low temperatures results in a sharp increase of the recombination rate and carrier lifetimes drop to tens of nanoseconds.<sup>21</sup> The mechanism behind this abrupt and sudden change has proven to be difficult to pin down.

<sup>a</sup> Department of Physics, School of Natural Sciences, University of California, Merced, CA 95344, USA. E-mail: sghosh@ucmerced.edu

<sup>b</sup> School of Engineering, University of California, Merced, CA 95344, USA

† Electronic supplementary information (ESI) available. See DOI: 10.1039/c6cp02971j

Another aspect where both anomalies and possible answers were highlighted by spectroscopic measurements is with regard to the excitonic binding energy ( $E_B$ ). It is typically evaluated to be anywhere in the range 30–100 meV from PL<sup>22</sup> and photo-absorption data,<sup>25</sup> an indication that a considerable fraction of excitons must be present at room temperature (an equivalent of 25 meV). But experiments have shown that room temperature PL is dominated by free charge carriers.<sup>25</sup> Magneto-absorption measurements have shown empirical evidence that  $E_B$  is temperature dependent, decreasing to 6 meV by 300 K.<sup>26</sup> This has been posited as a reason why hybrid PVSKs are unstable under ambient conditions, a subject at the very root of the biggest hindrance to their commercial viability. The value of a thorough investigation of the PVSK phase space is therefore not limited to pedagogical interests, but essential for critical insights into fundamental properties that will allow rational design and fabrication to extract the best performances.

We focus on static and dynamic PL spectroscopy of hybrid halide organic PVSKs fabricated using a high throughput and potentially scalable continuous liquid interface propagation (CLIP) technique<sup>27,28</sup> that has produced uniform thin films and demonstrated improved sample stability, often extending to weeks under ambient conditions. Using extensive temperature-dependent static and time-resolved spectroscopy, we have addressed several unresolved issues. First, we have systemically quantified the carrier recombination with temperature in the region < 140 K. These measurements show that charge lifetimes decrease with decreasing temperature, unusual for semiconductors, but indicative of radiative excitonic recombination. Next, by monitoring photoluminescence emission as a function of excitation power, we have demonstrated that the sudden increase in recombination rates accompanying the phase transition is related to the nature of the dominant charge carriers, which switch over from free electrons and holes to excitons. Additionally, we have developed a theoretical approach that allows estimation of the exciton binding energy directly from spectroscopic data. And finally, we have established a simple and direct technique to gauge PVSK film quality, a finding that will be of significant use in device design and development.

## 2. Experimental techniques

PVSK thin films are deposited on an indium tin oxide (ITO) substrate using the CLIP technique previously reported by our groups.<sup>27</sup> Methylammonium iodide (MAI) and lead(II) chloride ( $\text{PbCl}_2$ ) are uniformly dispersed in anhydrous dimethyl sulfoxide (DMSO) and *N*-methyl-2-pyrrolidione (NMP) (4 : 6, v/v) at a concentration of 2.64 M and 0.88 M, respectively. The ITO substrates are treated by UV/ozone prior to deposition for 20 min to improve the wettability. The precursor solution is electrohydrodynamically sprayed and kept aside in a Petri dish for 15 min, followed by annealing using a heat gun until the colour of the thin films changed to dark brown. Scanning electron microscope (SEM) images of the sample [Fig. S1a and b, ESI†] show both the uniformity and large crystal grains on the order of almost 10  $\mu\text{m}$ . Specifically, the cross-sectional SEM

image [Fig. S1(c), ESI†], reveals a continuous, single-slab like grain in the out-of-plane direction. For optical measurements we use two excitation sources: a pulsed supercontinuum source (NKT Photonics) and a continuous wave diode laser tuned to 532 nm (Coherent Inc.). The PL data are taken using an Acton 300i spectrometer and then dispersed onto a thermoelectrically cooled charge-coupled device with a spectral resolution of 0.18 nm. For the time-resolved measurements we use a time-correlated single photon counting (TCSPC) system (Picoquant) in conjunction with a supercontinuum source that allows us to vary the repetition rate. The temperature dependent measurements are done in a cryo-free system from Advanced Research Systems with a base temperature of 10 K.

## 3. Results and discussion

The results of optical characterization of the tetragonal structure above the phase transition ( $T > 120$  K) are summarized in Fig. 1. At room temperature, the emission is centred on 1.6 eV. As  $T$  is lowered, the emission spectrum narrows and red-shifts [Fig. 1(a)]. Fitting the spectrally integrated PL intensity ( $I_{\text{PL}}$ ) with temperature using  $I_{\text{PL}}(T) = I_0/[1 + A \exp(-E_B/k_B T)]$  allows us to extract  $E_B = 105 \pm 3$  meV [Fig. 1(b)]. However, it has been suggested that this approach of predicting  $E_B$  is inaccurate, as emission at different temperatures has contributions from varying proportions of excitons and free charge carriers.<sup>25</sup>

The rate of change of the exciton and free charge carrier concentration can be explicitly written as:

$$\frac{\partial n}{\partial t} = -(1 - \gamma)Rnp - \gamma Rnp + K_d X$$

$$\frac{\partial p}{\partial t} = -(1 - \gamma)Rnp - \gamma Rnp + K_d X$$

$$\frac{\partial X}{\partial t} = -K_d X - K_r X + G + \gamma Rnp - R_{nr}$$

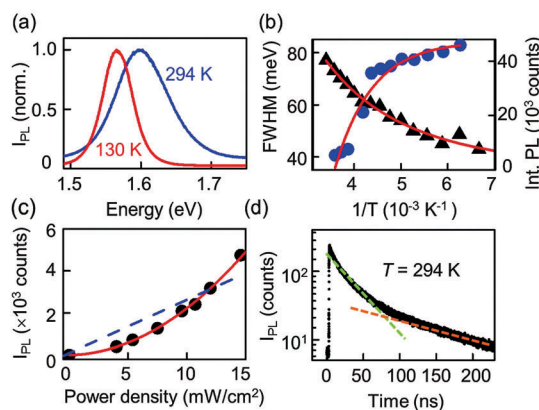


Fig. 1 (a) Temperature dependent emission of the tetragonal phase. (b) Peak full-width at half maxima (FWHM, triangles) and spectrally integrated emission intensity (circles) varying with temperature  $T$ . The fits are discussed in the text. (c) Spectrally-integrated PL at 294 K as a function of excitation power density. The lines compare linear (dashed) and quadratic (solid) fits to the data. (d) Time-resolved emission on a semi-log scale showing two distinct lifetimes in the tetragonal phase.

where  $n$ ,  $p$  and  $X$  are the electron, hole and exciton concentrations, respectively,  $R$  is the recombination rate of electrons and holes,  $\gamma$  is the proportion of electrons and holes recombining to form excitons,  $K_d$  is the exciton dissociation rate,  $G$  is the exciton generation rate, and  $K_r$  and  $R_{nr}$  are the rates of radiative and non-radiative exciton recombination. At the excitation powers used the non-radiative sites are saturated, and hence the non-radiative rate may be considered to be constant. Generation of free charge carriers is solely attributed to exciton dissociation. Charge trapping is not considered to be a contributing factor, as the extent of any unintentional doping is negligible compared to the photo-excited carrier concentration ( $\sim 10^{15} \text{ cm}^{-3}$ ). Nor are exciton–exciton interactions, as they are noticeable only at a high free carrier concentration ( $> 10^{21} \text{ cm}^{-3}$ ). Under continuously pulsed illumination it is safe to assume that all the generated charge carriers recombine and the dissociation of excitons to holes and electrons to be in dynamic equilibrium. Since the electron–hole recombination ( $R_{np}$ ) is proportional to the photo-generated densities of the electrons and holes and the exciton radiative recombination ( $K_r X$ ) is proportional to the exciton concentration, we get

$$I_{\text{PL}} \sim x^2 [N_{\text{tot}}]^2 + (1 - x - k) N_{\text{tot}}$$

where  $I_{\text{PL}}$  is the spectrally integrated emission and  $x$  is the fraction of free carriers.  $(1 - x - k)$  is the fraction of excitons that undergo radiative recombination, where  $k$  is the fractional population that contributes to non-radiative recombination.<sup>16–29</sup>  $N_{\text{tot}}$  is the total charge carrier concentration, which in turn is linearly proportional to the excitation power  $P$ . Thus, the contribution of the free carrier recombination to the emission leads to  $I_{\text{PL}} \propto P^2$ , while the corresponding contribution from exciton recombination will show up as  $I_{\text{PL}} \propto P$ . Therefore, we can estimate the relative fraction of free carriers and excitons by fitting a second order polynomial to data as shown in Fig. 1(c). The square root of the quadratic part represents the fraction of electrons/holes and the linear part corresponds to the fraction of excitons undergoing radiative recombination. Using this method, we can accurately estimate the fraction of excitons, utilizing the internal quantum efficiency spectra of these films.<sup>16–29</sup> For example, a clear quadratic dependence of the data at 294 K as shown in Fig. 1(c) suggests that the emission is a result of recombination of mostly free carriers and not excitons, though there might still be excitons undergoing non-radiative recombination.

We begin our investigation into the low temperature phase space by studying the PL at the initiation of the structural transition from tetragonal-to-orthorhombic phase and map the spectra as functions of emission energy and temperature in Fig. 2(a). Unlike the behaviour at  $T > 120$  K, the tetragonal emission (centred on 1.59 eV at 120 K) now blue-shifts and broadens considerably between 120–100 K. At 90 K it merges with an emerging low energy side-band, while the orthorhombic peak (1.65 eV) dominates the spectral signature. On lowering the temperature further, the orthorhombic peak is clearly visible and the spectral region enclosed by the dashed box still shows a weak emission from the tetragonal phase. The relative novelty of hybrid PVSKs means that the energy states of these systems are

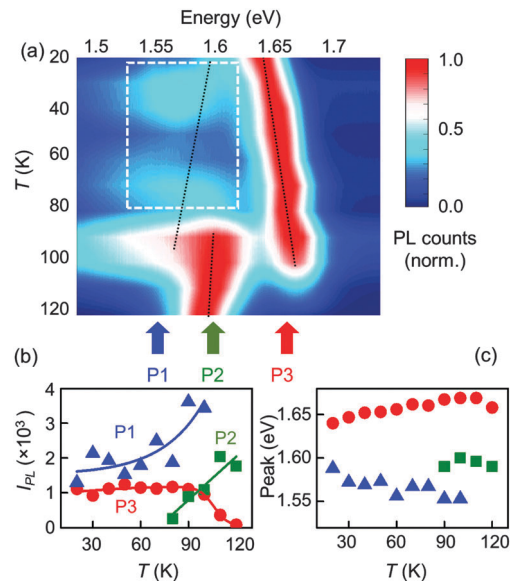
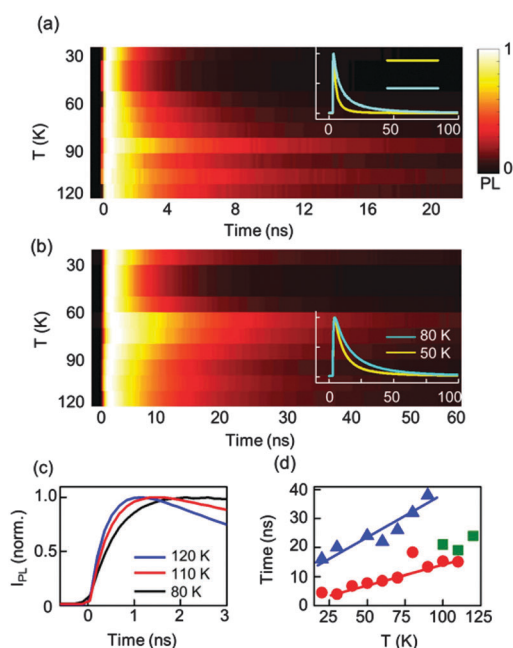


Fig. 2 (a) PL intensity mapped with emission energy and temperature. Arrows highlight the spectral positions of peaks under investigation for  $T < 120$  K, dashed lines show the position of peaks. (b) Spectrally integrated PL and (c) centre wavelength of the peaks shown in part (a) varying with temperature.

not definitively understood yet. Using this PL data we have summarized our results to sketch an energy level diagram in Fig. S2(b) (ESI<sup>†</sup>). The persistence of the tetragonal phase at low  $T$  is supported by absorption data.<sup>25</sup> For a quantitative analysis, we fit the emission over the entire energy range using three Gaussian distributions (see Fig. S2, ESI<sup>†</sup>), centred about the emission energies designated as P1–P3 at 120 K, which means these are not fixed peak positions, but rather, identify the starting points. The integrated emission intensity and peak position of each of these are plotted with  $T$  in Fig. 2(b) and (c), respectively. The data for P3 in Fig. 2(b) shows that after the phase transition progresses to completion at  $T = 90$  K, the spectral weight associated with this peak is unchanged down to 10 K, while its spectral position in Fig. 2(c) shows a minor red-shift with decreasing  $T$ . The results of the analysis of P1 and P2 are more complex and illuminating. P2 centres on the tetragonal emission and its spectral weight decreases steadily, disappearing by  $T \sim 80$  K in Fig. 2(b). Its peak position in Fig. 2(c) shows no discernible variation between 120 K and 80 K. The demise of P2 is accompanied by the emergence of a broad sideband, labelled P1, at  $T = 100$  K, but this too quenches with decreasing temperature, as seen in Fig. 2(b). Its peak positions in Fig. 2(c), however, show that while the sideband emerges separate from the tetragonal peak at first, for  $T < 90$  K it is likely that P1 is a contribution from remnants of the tetragonal phase after all.

The most striking spectroscopic change that accompanies the structural transition is in the PL recombination rates across the entire spectral range. The time-resolved PL at  $T = 294$  K [Fig. 1(d)] shows a bi-exponential decay with long and short lifetimes of 186 and 24 ns, respectively, corresponding to an

average recombination lifetime of  $169 \pm 2.4$  ns, and this persists till  $T = 130$  K (Fig. S3, ESI<sup>†</sup>). At  $T = 120$  K the recombination lifetime drops abruptly and drastically by an order of magnitude, a result that has been previously observed but not studied systematically or in-depth, and consequently, not fully elucidated. One proposition is an energy transfer process where the carriers of the high-energy orthorhombic phase may diffuse to the small inclusions of the persisting tetragonal phase that provide a low energy channel for recombination.<sup>21</sup> The co-existence of two phases has been observed in a number of systems before and the smaller inclusions are stabilized due to the strain or pressure developed within the films.<sup>30,31</sup> These inclusions could be a result of lattice-mismatch or lattice defects in the high temperature phase that induce spontaneous plane shifts during phase transition in the films, and can have major effects on the film conductivity and other photovoltaic properties.<sup>30,31</sup> Due to extensive scattering at these lattice boundaries originating from randomly oriented lattices, there will be increased resistance and lowered mobility of charge carriers.<sup>32</sup> These locations have also been observed as electron trapping sites in magnesium oxide (MgO) films and hence minimizing these mismatch sites or defects is of paramount importance to enhance film quality.<sup>33</sup> In Fig. 3 we highlight our results of the spectrally-resolved time-resolved PL in the range of 120–10 K. Fig. 3(a) maps the PL as a function of time and temperature, with the '0' on the time axis demarcating the arrival of the excitation pulse for emission peak P3, which we can tie to the PL from just the orthorhombic phase. Fig. 3(b) shows the corresponding data for emission from the low



**Fig. 3** Time-resolved PL data mapped with temperature and time for (a) high energy peak, P3 and (b) low energy states (P1 and P2). (insets) Sample time traces. (c) Initial rise of the time-resolved PL for low energy states at different temperatures. (d) Recombination lifetimes extracted from exponential fits to data in (a) and (b) with symbols corresponding to peaks in Fig. 2(b). Fit errors are 0.17 ns for (a) and 0.015 ns for (b).

energy states which is peak P2 for temperatures between 120 K and 100 K, and P1 for  $T < 100$  K. The insets in both these figures show representative time-resolved PL traces at 80 and 50 K. Comparing the two data sets, the most noticeable observation is how much faster the recombination at the orthorhombic site is than that from the lower energy states associated with the tetragonal phase. This gives credence to the hypothesis that there is energy transfer from the high to low energy sites. Fig. 3(c) shows the first 3 ns following the arrival of the excitation pulse for the low energy states. The observed initial rise, which slows with decreasing  $T$ , is a charging time denoting signal build-up as carriers arrive from the high energy state, providing further confirmation. In cases of such incoherent energy transfer, the recombination times of the high energy states are reduced from their normal value as carriers migrate to the low energy sites and recombine there instead. This is observed very clearly in ensembles of semiconducting quantum dots,<sup>34</sup> and the result is a monotonic increase of recombination times as the emission energy decreases. However, the longest lifetime observed at the lowest energies is never longer than the native unaltered lifetime of the system. Therefore, while there is definitely some aspect of energy transfer between the close-lying low temperature states in the hybrid PVSKs, there could also be variations in intrinsic charge carrier dynamics of the films due to the presence of high temperature nano-scale domains that could further lead to the faster recombination. It does not explain at all why the recombination from the remnants of the tetragonal phase should have such a highly reduced lifetime as well. Studying the change in optical properties and charge carrier dynamics will be an effective tool to characterize these lattice defects and will be a check for film quality. As Fig. 3(d) demonstrates, the recombination times show further variations with decreasing temperature. The orthorhombic emission decays faster as  $T$  decreases. And for  $T < 100$  K, the low energy PL shows an even steeper reduction. This decrease of lifetimes as  $T$  is lowered, while unusual in direct band-gap semiconductors where reduced phonon coupling to photo-generated carriers increases charge lifetimes, is an indication of the emission PL being dominated by radiative excitonic recombination.

In an effort to explain these changes in carrier dynamics, we focus on the type of carriers that lead to recombination at different temperatures. In Fig. 4(a) we plot the variation of  $I_{PL}$  with  $P$  at different temperatures, fit the data with a second order polynomial and compare the linear and quadratic coefficients of these fits in Fig. 4(b). As expected, at  $T = 294$  K the quadratic component is responsible for almost the entire weight, confirming that radiative recombination is driven entirely by free carriers and the exciton fraction solely comes from the nonradiative part. However, at 200 K there is a linear component that accounts for almost 25% of the total weight, implying the radiative recombination of both free carriers and excitons, with the majority still being the former. By 80 K the majority component in  $I_{PL}$  is linear, accounting for 60% of the total weight. Based on this monotonic change with  $T$  we conclude that there is a crossover from free carriers to exciton-dominated radiative recombination, and in Fig. 4(c) the calculated free

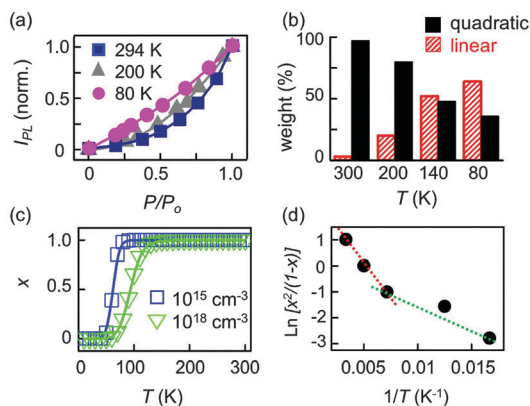


Fig. 4 (a) Integrated PL counts varying with excitation power at  $T = 294$ , 200 and 80 K for the peak designated P2 in Fig. 2(a). Lines are polynomial fits ( $*R^2$  value = 0.99). (b) The relative weight of the linear (shaded) and quadratic (solid) components derived from the fits in (a). (c) Calculated fraction of free carriers as a function of  $T$  for  $E_B = 100$  meV,  $n = 10^{18}$   $\text{cm}^{-3}$  and  $n = 10^{15}$   $\text{cm}^{-3}$ . (d) Calculated exciton binding energy varying with  $T$  ( $R^2$  = coefficient of determination).

charge carriers using the Saha–Langmuir equation is plotted for an exciton binding energy of 100 meV. The Saha–Langmuir equation,<sup>35,36</sup> derived in the context of ionization of gases, provides a relationship between this fraction  $x$  and temperature  $T$  for a constant ‘ionization’ energy, which in this case is  $E_B$ . The calculated  $x$  with  $T$  for  $E_B = 100$  meV and electron carrier density  $n = 10^{15}$   $\text{cm}^{-3}$  (squares) underestimates the crossover  $T$  considerably. Our experimental parameters indicate a carrier density in the range of  $10^{15}$ – $10^{16}$   $\text{cm}^{-3}$ , but we re-calculate by increasing the free carrier concentration to  $n = 10^{18}$   $\text{cm}^{-3}$  (triangles), which moves the crossover  $T$  higher, but does not replicate the experimental fractions of charge carriers. In fact, there exists no reasonable combination of  $E_B$  and  $n$  that can mimic the experimental  $x$ . We therefore consider more closely the statistical mechanics underlying the dissociation of the excitons into electron–hole pairs.

The equilibrium constant for this reaction  $\text{exc} \rightleftharpoons \text{e} + \text{h}$  is given by  $K = (N_e N_h) / N_{\text{exc}}$ . The corresponding free energy  $\Delta G$  is:

$$\Delta G = -k_B T \ln K = -k_B T \ln [x^2 / (1-x) N_{\text{tot}}]$$

where  $N_{\text{tot}}$  is the total number of all carriers (free electrons/holes and excitons). Rearranging, we arrive at:

$$\ln [x^2 / (1-x)] = -\Delta G / k_B T - \ln N_{\text{tot}}$$

This is the form of a standard Van’t Hoff plot,<sup>37</sup> and is shown in Fig. 4(d), where we plot  $\ln[K]$  as a function of  $1/T$ . In order to calculate the total exciton concentration  $(1-x)$ , we will need to find the fraction undergoing non-radiative recombination. From the IQE spectra reported by our group,<sup>27,28</sup> we can estimate it to be 0.2 in the 500–680 nm wavelength range. This value is a constant and does not vary with temperature as all the recombination sites are occupied. The slope of this plot yields the change in free energy,  $-\Delta G$ , and therefore, leads us to the following conclusions: (a) the slope is negative, implying that

the change in free energy is positive, *i.e.*, energy is needed to dissociate excitons, an expected result; and (b) the slope changes with  $T$ , and has a larger negative value in the low temperature phase compared to the high temperature phase, indicated by dotted lines in Fig. 4(d), which clearly shows that the binding energy is different in the two temperature regimes. We now use this measured free energy to calculate the exciton binding energy as follows:

$$\Delta G = -k_B T \ln [Z_e Z_h / Z_{\text{exc}}] = -k_B T \ln \left[ \exp(-E_B / k_B T) \frac{Z_e^* Z_h^*}{Z_{\text{exc}}^*} \right]$$

and

$$\Delta G = E_B - k_B T \ln \left[ \frac{Z_e^* Z_h^*}{Z_{\text{exc}}^*} \right]$$

where  $*$  denotes the translational partition functions. For an ideal gas  $Z^* = (Z_e^* Z_h^*) / (Z_{\text{exc}}^*) = ((2\pi m^* k_B T) / h^2)^{3/2} V$ , and  $m^* = (m_e m_h) / m_{\text{exc}}$  and we use a numerical value of 0.1  $m_e$ . Combining the above equations while keeping  $E_B$  constant, yields the Saha equation. The calculated  $E_B$  for the high temperature phase had an average value of 95 meV and the low temperature phase had a value of 45 meV. The reason for the change in binding energy could be due to band bending at the domain boundaries, and hence the change could be a convenient indicator of these domains, which indirectly helps us determine the amount of lattice defects in the films.

## 4. Conclusions

Hybrid PVSks show great promise for a variety of applications, making it imperative that we invest in understanding their fundamental properties. We have used low temperature spectroscopy to study the phase space of  $\text{CH}_3\text{NH}_3\text{PbI}_{3-x}\text{Cl}_x$  and our results demonstrate that the notable spectral and dynamic changes that accompany the structural phase transition occur due to the presence of domains in the low temperature phase. These low temperature domains can be an effective way to characterize lattice defects in the high temperature film. We use the variation of spectrally integrated PL with excitation power to estimate the proportion of each carrier type at different temperatures and apply fundamental statistical physics principles to calculate  $E_B$  from these data. We calculated the average  $E_B$  values in the two temperature regimes and found the high temperature value (95 meV) to be very close to the numerical value of 105 meV derived from a fit to temperature dependent PL data. This leads us to conclude that the typical approach to measure  $E_B$  gives us an average value, while evaluating the PL at specific temperatures over a range of excitation powers offers a more accurate result. This change in binding energy indirectly lets us estimate film defects in the high temperature phase and can be an effective check of film quality. We have also developed a direct method to estimate the binding energy of excitons in hybrid PVSks. Our approach provides a route towards checking films for lattice defects and ensuring the high quality necessary for superior performance and will assist greatly in ongoing materials engineering efforts to minimize defects and electron

trapping sites, therefore making the application of PVSK photo-voltaics a reality.

## Acknowledgements

This research was supported by funds from the National Aeronautics and Space Administration (NASA) grant no. NNX15AQ01A, and National Science Foundation (NSF) grant no. DMR-1056860 and ECC-1227034. V. T. gratefully acknowledges the support of user proposals (#3192 and #3715) at the Molecular Foundry, Lawrence Berkeley National Lab, supported by the Office of Basic Energy Sciences, of the U.S. Department of Energy under grant no. DE-AC02-05CH11231, and A. G. acknowledges support from a James S. McDonnell Foundation Award.

## Notes and references

- 1 A. Kojima, K. Teshima, Y. Shirai and T. Miyasaka, *J. Am. Chem. Soc.*, 2009, **131**, 6050–6051.
- 2 N. J. Jeon, J. H. Noh, W. S. Yang, Y. C. Kim, S. Ryu, J. Seo and S. I. Seok, *Nature*, 2015, **517**, 476–480.
- 3 H. Zhou, Q. Chen, G. Li, S. Luo, T. B. Song, H. S. Duan, Z. Hong, J. You, Y. Liu and Y. Yang, *Science*, 2014, **345**, 542–546.
- 4 W. Nie, H. Tsai, R. Asadpour, J. C. Blancon, A. J. Neukirch, G. Gupta, J. J. Crochet, M. Chhowalla, S. Tretiak, M. A. Alam, H. L. Wang and A. D. Mohite, *Science*, 2015, **347**, 522–525.
- 5 H.-S. Kim, I. Mora-Sero, V. Gonzalez-Pedro, F. Fabregat-Santiago, E. J. Juarez-Perez, N.-G. Park and J. Bisquert, *Nat. Commun.*, 2013, **4**, 2242, DOI: 10.1038/ncomms3242.
- 6 C. Wehrenfennig, G. E. Eperon, M. B. Johnston, H. J. Snaith and L. M. Herz, *Adv. Mater.*, 2014, **26**, 1584–1589.
- 7 C. S. Ponce Jr, T. J. Savenije, M. Abdellah, K. Zheng, A. Yartsev, T. Pascher, T. Harlang, P. Chabera, T. Pullerits, A. Stepanov, J. P. Wolf and V. Sundstrom, *J. Am. Chem. Soc.*, 2014, **136**, 5189–5192.
- 8 S. D. Stranks, G. E. Eperon, G. Grancini, C. Menelaou, M. J. Alcocer, T. Leijtens, L. M. Herz, A. Petrozza and H. J. Snaith, *Science*, 2013, **342**, 341–344.
- 9 M. I. Dar, N. Arora, P. Gao, S. Ahmad, M. Gratzel and M. K. Nazeeruddin, *Nano Lett.*, 2014, **14**, 6991–6996.
- 10 Z. K. Tan, R. S. Moghaddam, M. L. Lai, P. Docampo, R. Higler, F. Deschler, M. Price, A. Sadhanala, L. M. Pazos, D. Credgington, F. Hanusch, T. Bein, H. J. Snaith and R. H. Friend, *Nat. Nanotechnol.*, 2014, **9**, 687–692.
- 11 H. J. Snaith and L. Schmidt-Mende, *APL Mater.*, 2014, **2**, 081201.
- 12 A. Abate, M. Saliba, D. J. Hollman, S. D. Stranks, K. Wojciechowski, R. Avolio, G. Grancini, A. Petrozza and H. J. Snaith, *Nano Lett.*, 2014, **14**, 3247–3254.
- 13 M. Liu, M. B. Johnston and H. J. Snaith, *Nature*, 2013, **501**, 395–398.
- 14 D. Shi, V. Adinolfi, R. Comin, M. Yuan, E. Alarousu, A. Buin, Y. Chen, S. Hoogland, A. Rothenberger, K. Katsiev, Y. Losovyj, X. Zhang, P. A. Dowben, O. F. Mohammed, E. H. Sargent and O. M. Bakr, *Science*, 2015, **347**, 519–522.
- 15 J. Troughton, C. Charbonneau, M. J. Carnie, M. L. Davies, D. A. Worsley and T. M. Watson, *J. Mater. Chem. A*, 2015, **3**, 9123–9127.
- 16 Y. Yamada, T. Nakamura, M. Endo, A. Wakamiya and Y. Kanemitsu, *J. Am. Chem. Soc.*, 2014, **136**, 11610–11613.
- 17 F. Deschler, M. Price, S. Pathak, L. E. Klintberg, D. D. Jarausch, R. Higler, S. Huttner, T. Leijtens, S. D. Stranks, H. J. Snaith, M. Atature, R. T. Phillips and R. H. Friend, *J. Phys. Chem. Lett.*, 2014, **5**, 1421–1426.
- 18 C. Wehrenfennig, M. Liu, H. J. Snaith, M. B. Johnston and L. M. Herz, *J. Phys. Chem. Lett.*, 2014, **5**, 1300–1306.
- 19 Y.-C. Hsiao, T. Wu, M. Li and B. Hu, *J. Mater. Chem. A*, 2015, **3**, 15372–15385.
- 20 W. Kong, Z. Ye, Z. Qi, B. Zhang, M. Wang, A. Rahimi-Iman and H. Wu, *Phys. Chem. Chem. Phys.*, 2015, **17**, 16405–16411.
- 21 C. Wehrenfennig, M. Liu, H. J. Snaith, M. B. Johnston and L. M. Herz, *APL Mater.*, 2014, **2**, 081513.
- 22 K. Wu, A. Bera, C. Ma, Y. Du, Y. Yang, L. Li and T. Wu, *Phys. Chem. Chem. Phys.*, 2014, **16**, 22476–22481.
- 23 D. W. deQuilettes, S. M. Vorpahl, S. D. Stranks, H. Nagaoka, G. E. Eperon, M. E. Ziffer, H. J. Snaith and D. S. Ginger, *Science*, 2015, **348**, 683–686.
- 24 Y. Li, W. Yan, Y. Li, S. Wang, W. Wang, Z. Bian, L. Xiao and Q. Gong, *Sci. Rep.*, 2015, **5**, 14485, DOI: 10.1038/srep14485.
- 25 V. D'Innocenzo, G. Grancini, M. J. Alcocer, A. R. Kandada, S. D. Stranks, M. M. Lee, G. Lanzani, H. J. Snaith and A. Petrozza, *Nat. Commun.*, 2014, **5**, 3586, DOI: 10.1038/ncomms4586.
- 26 A. Miyata, A. Mitioglu, P. Plochocka, O. Portugall, J. Tse-Wei Wang, S. D. Stranks, H. J. Snaith and R. J. Nicholas, *Nat. Phys.*, 2015, **11**, 582–594.
- 27 H. Ishihara, W. Chen, Y.-C. Chen, S. Sarang, N. De Marco, O. Lin, D. Sun, W. L. Queen, S. Ghosh and V. C. Tung, *Adv. Mater. Interfaces*, 2016, **3**, DOI: 10.1002/admi.201500762.
- 28 H. Ishihara, S. Sarang, Y.-C. Chen, O. Lin, P. Phummirat, L. Thung, J. Hernandez, S. Ghosh and V. C. Tung, *J. Mater. Chem. A*, 2016, **4**, 6989–6997, DOI: 10.1039/C5TA09992G.
- 29 Y. Yamada, H. Yasuda, T. Tayagaki and Y. Kanemitsu, *Phys. Rev. Lett.*, 2009, **102**, 247401.
- 30 L. Ehm, L. A. Borkowski, J. B. Parise, S. Ghose and Z. Chen, *Appl. Phys. Lett.*, 2011, **98**, 021901.
- 31 Z. Chen, L. You, C. Huang, Y. Qi, J. Wang, T. Sritharan and L. Chen, *Appl. Phys. Lett.*, 2010, **96**, 252903, DOI: 10.1063/1.3456729.
- 32 S.-Z. Chang, T.-C. Chang, J.-L. Shen, S.-C. Lee and Y.-F. Chen, *J. Appl. Phys.*, 1993, **74**, 6912–6918.
- 33 H.-M. Benia, P. Myrach, A. Gonchar, T. Risse, N. Nilius and H.-J. Freund, *Phys. Rev. B: Condens. Matter Mater. Phys.*, 2010, **81**, 241415, DOI: 10.1103/PhysRevB.81.241415.
- 34 M. Lunz, A. L. Bradley, V. A. Gerard, S. J. Byrne, Y. K. Gun and V. L. K. N. Gaponik, *Phys. Rev. B: Condens. Matter Mater. Phys.*, 2011, **83**, 115423.
- 35 R. Cingolani, L. Calcagnile, G. Col', R. Rinaldi, M. Lomoscio, M. DiDio, A. Franciosi, L. Vanzetti, G. C. LaRocca and D. Campi, *J. Opt. Soc. Am. B*, 1996, **13**, 1268–1277.
- 36 M. N. Saha, *Proc. R. Soc. A*, 1921, **99**, 135–153.
- 37 P. Atkins and J. De Paula, *Physical Chemistry*, W. H. Freeman and Company, 8th edn, 2006.